RSC Advances

PAPER

View Article Online
View Journal | View Issue

Cite this: *RSC Adv.*, 2021, **11**, 7961

Effect of dopant concentration and the role of ZnS shell on optical properties of Sm^{3+} doped CdS quantum dots

N. D. Vinh,[a] P. M. Tan,[b] P. V. Do,[c] S. Bharti,[d] V. X. Hoa,[e] N. T. Hien,[e] N. T. Luyen[e] and N. X. Ca*[e]

The role of samarium (Sm) dopant on the structural, morphological, and optical properties of CdS QDs and CdS/ZnS core/shell QDs was methodically reported. The synthesis of Sm-doped CdS QDs and CdS/ZnS QDs was carried out *via* a facile wet chemical method. The structure, chemical composition, and optical properties of the synthesized QDs were investigated by using X-ray diffraction (XRD), X-ray photoelectron spectroscopy (XPS), Raman spectroscopy (RS), and photoluminescence (PL) spectroscopy. XRD analysis showed that the synthesized CdS QDs exhibited zinc blende structure which was not affected by doping Sm^{3+} ions. The particle size of the CdS:Sm and CdS:Sm (2%)/ZnS QDs was estimated to be ~4 nm and ~7 nm, respectively. Transmission electron microscopy (TEM) images revealed that the incorporation of Sm dopant did not significantly affect the size and morphology of CdS QDs, while the formation of the ZnS shell increased the particle size. XPS and XRD results confirmed the successful incorporation of Sm^{3+} ions into the CdS QDs. The effect of dopant concentration on the structural and luminescent properties was studied. The emission and excitation spectra of Sm^{3+}-doped CdS QDs and CdS/ZnS QDs consisted of the characteristic lines corresponding to the intra-configurational f–f transitions. The energy transfer (ET) mechanism from the host to Sm^{3+} ions and the ET process through cross-relaxation between Sm^{3+} ions have been elucidated. The effect of the ZnS shell on the optical stability of the Sm^{3+}-doped CdS QDs was studied in detail and the results showed that the CdS:Sm (2%)/ZnS QDs retained their good emission characteristics after 376 days of fabrication. The luminescent properties of Sm-doped QDs ranging from violet to red and PL lifetime extending to milliseconds demonstrated that these QDs are the potential materials for applications in white LEDs, biomarkers, and photocatalysis.

Received 21st September 2020
Accepted 2nd February 2021

DOI: 10.1039/d0ra08056j

rsc.li/rsc-advances

1. Introduction

Nanostructures have always attracted the interest of researchers because of their unique tunable properties and their potential in fundamental studies and technical applications. Semiconductor materials of the II–VI group are an important class of nanomaterials owing to their distinctive optoelectronic properties. Cadmium sulfide (CdS) is one of the n-type striking material with a narrow bandgap of 2.42 eV and potential applications in the optical and electronic industries.[1,2] CdS is of high interest to researchers because of its intrinsic conduction band position, relatively high nonlinear optical response, and photocatalytic activity.[3,4] Inorganic quantum dots (QDs) have a quantum efficiency of 20–80% and are stable under a harsh environment. Semiconductor QDs possess broad and continuous absorption spectra, whereas the emission spectra are narrow and independent of the excitation wavelength. However, naked CdS nanostructures have various limitations including photo-corrosion, high carrier recombination rate, and limited active sites.[5–7]

The optical properties of II–VI semiconductors can be enhanced by various methods like optical annealing, luminescent ion doping, and coating with a higher bandgap material.[8–10] The coating of CdS nanostructures with a higher bandgap material can enhance the photoluminescence quantum yield and photostability because the surface non-radiative recombination defects are eliminated and the dangling bonds are reduced. Several studies have focused on the synthesis and improvement of optical properties of Type-I core/shell nanostructures such as CdSe/CdS, CdSe/ZnS, and CdS/ZnS, *etc.* CdS and ZnS have a similar crystalline structure, which makes them interesting for optoelectronic and biological applications.[11,12] ZnS is the most chosen semiconductor

[a]*Faculty of Chemistry, TNU – University of Sciences, Thai Nguyen, Vietnam*
[b]*Faculty of Fundamental Sciences, Thai Nguyen University of Technology, Thai Nguyen, Vietnam*
[c]*Thuyloi University, 175 Tay Son, Dong Da, Hanoi, Vietnam*
[d]*Panjab University, Chandigarh, 160014, India*
[e]*Faculty of Physics and Technology, TNU – University of Sciences, Thai Nguyen, Vietnam. E-mail: canx@tnus.edu.vn*

material for shell formation because it can enhance the fluorescent efficiency and reduce the toxicity of the unstable core. ZnS can improve the chemical and optical stability by acting as an anti-oxidant layer and shield the reactive core from photobleaching and the outer environment.[13] In Type-I core/shell nanostructures, the holes and electrons are confined in the core and the shell does not contribute much to the wavefunction.[14]

Doping semiconductor QDs with a suitable material is an important approach utilized in the nanotechnology field for modifying the material properties.[15] Effective doping can not only modify the electronic, structural, and optical properties of the host material but also enhance the photocatalytic properties of semiconductor nanostructure. In addition to the different synthesis approaches such as varying solvents and precursors and changing temperature which have been applied to modify the key properties of CdS QDs, the doping of the proper material is also an important route.[16,17]

Doping of lanthanides is a novel approach that has been received a lot of attention. Owing to the unique electrical, optical and chemical properties, lanthanides have great potential for applications such as luminescent devices, color displays, optical communication, and catalysts. The photocatalytic activity of the doped material increases because doping provides a path to concentrate the target molecules (organic pollutants) at the catalyst surface by forming a Lewis acid–base complex.[18] Lanthanides cause the effective separation of e^-–h^+ pairs and increase the light sensitivity of the photocatalyst.[19,20] The electronic structure of lanthanides is special, thus, they can form complex with Lewis bases like aldehydes, acids, and alcohols very easily.

Among various lanthanides, samarium (Sm) is of particular interest for phosphor applications because of its multiple energy level structures and high emission spectra. Sm has high potential in color displays, optical data storage, optical amplifiers, underwater communication, *etc.*[21–23] The characteristic that makes this material highly interesting is the strong luminescence in the visible spectrum exhibited by Sm^{3+} ions and the emitting $^4G_{5/2}$ energy level with a relatively high quantum efficiency.[24] Researchers have synthesized Sm^{3+}-doped TiO_2 and ZnO nanostructures[25,26] and found that Sm^{3+} ions could enhance the visible light absorption of TiO_2 and ZnO nanostructures, leading to the improvement of the photocatalytic activity. Therefore, II–VI semiconductor QDs doped with lanthanides have been potentially applied in various areas such as display production, electronic device manufacture, and biomedical technology. To our best knowledge, the works with the synthesis of Sm-doped semiconductor CdS QDs and Sm-doped CdS/ZnS core/shell QDs and their properties have been carried out limitedly until now.

The present paper reports the effect of Sm doping on CdS QDs and core/shell CdS/ZnS QDs. A wet chemical method is used to synthesize CdS QDs and CdS/ZnS QDs doped with Sm ions. CdS QDs are doped with different concentrations of Sm (0.5–2%) and are systematically studied for their structure, optical properties, and morphology. The effect of Sm doping on CdS/ZnS core/shell QDs has been explored using various spectroscopic techniques. The structure and chemical composition of all samples are investigated by XRD, TEM, RS, and XPS. The optical properties of the synthesized samples are studied by using PL and PL excitation (PLE) spectroscopy. The ET mechanism from host to dopant and the ET process through cross-relaxation between Sm^{3+} ions are elucidated. The emission decay curve is studied to explore the decay lifetime of the synthesized QDs.

2. Experimental

2.1. Materials

The chemicals and solvents used throughout the experiments were of analytical grade and used directly without any further purification. Cadmium oxide (CdO, 99.99%, powder), sulfur (S, 99.98%), samarium(III) acetate hydrate ($Sm(CH_3COO)_3 \cdot H_2O$, 99.9%), oleic acid (OA, 90%), Tri-*n*-octylphosphine (TOP, 97%), 1-octadecene (ODE, 90%), toluene (99.8%) and isopropanol (99.7%) were purchased from Sigma-Aldrich.

2.2. Synthesis of Sm-doped CdS and CdS/ZnS QDs

The synthesis process used to fabricate Sm-doped CdS QDs and Sm-doped CdS/ZnS core/shell QDs was adapted and modified according to the process reported in our studies.[27,28] In a three-neck flask, 128 mg of CdO powder was dissolved in a mixture of 2 ml of OA and 20 ml of ODE at 240 °C under a continuously stirring condition to produce a homogeneous Cd^{2+} ion solution. A solution containing S^{2-} ions was prepared by mixing 32 mg of S with 5 ml of ODE and 1 ml of TOP solution at 100 °C. $Sm(CH_3COO)_3 \cdot H_2O$ was dissolved in TOP and ODE and stirred at 150 °C until a homogeneous clear solution of Sm^{3+} was obtained. The precursor solutions containing Cd^{2+} ions and Sm^{3+} ions were mixed with different Sm^{3+}/Cd^{2+} ratios (the concentrations of Sm^{3+} ions used for doping CdS QDs were 0.5%, 1%, and 2%). Then, the S^{2-} solution was added quickly to the mixture containing Cd^{2+} and Sm^{3+} ions at 240 °C. For the nucleus growth of Sm-doped CdS QDs, the reaction system was maintained at 240 °C for 60 min. The fabricated Sm-doped CdS QDs were dispersed in isopropanol to remove extra unreacted Cd^{2+}, Sm^{3+}, and S^{2-} ions and separated from the liquid by centrifuging. The purified Sm-doped CdS QDs were re-dispersed in toluene and ODE and the obtained mixture was used for ZnS coating experiments.

For the formation of ZnS shell over Sm-doped CdS QDs, ZnO, and S were used to prepare Zn^{2+} and S^{2-} precursor solutions. For the S^{2-} precursor, 32 mg of S was dissolved in 1 ml of TOP and 5 ml of ODE solvent at 100 °C and for the Zn precursor, 81 mg of ZnO was dissolved in a mixture consisting of 2 ml of OA and 5 ml of ODE at 200 °C. The solutions containing Zn^{2+} and S^{2-} ions were slowly added to previously prepared Sm-doped CdS QDs at 220 °C. This solution was left for 30 min to grow the ZnS shell. For the purification process, QDs were separated from the solvent by centrifuging at 10 000 rpm for 5 min. The obtained QDs were dispersed in toluene for further characterizations. All of the synthesis processes were performed in nitrogen ambiance to avoid oxidation.

3. Characterization

To study the optical properties of the fabricated QDs, emission and excitation spectra, and luminescent lifetime were measured

using an FLS1000 system (Edingburgh, UK) with a 450 W Xe lamp at room temperature. The crystal structure of the fabricated samples was analyzed using an X-ray diffractometer (Siemens, D5005) equipped with a Cu-Kα radiation source. The morphology of the QDs was observed using TEM (JOEL-JEM 1010) operated at 80 kV. X-ray photoelectron spectroscopy (XPS) measurements were performed on a Thermo VG Escalab 250 photoelectron spectrometer. Raman spectra (RS) were measured using a LABRAM-HR800 spectrometer (Horriba, Jobin Yvon) with a wavelength $\lambda_{exc} = 488$ nm (2.54 eV) generated from an Ar^+ laser as an excitation source. To compare the emission intensity and avoid the re-absorption, the optical density of the samples was normalized (equal to 0.07) at the excitation wavelength 378 nm.

4. Results and discussion

4.1. Morphology and structural analysis

4.1.1. TEM micrograph. TEM images of (a) CdS QDs, (b) CdS:Sm (2%) QDs and (c) CdS:Sm (2%)/ZnS core/shell QDs are given in Fig. 1. The synthesized CdS QDs and CdS:Sm (2%) QDs are nearly spherical and homogeneously dispersed with an average size of 4 nm and there is no agglomeration of these QDs. It is clear that when the CdS QDs were doped with 2% of Sm, their surface morphology and size are similar to those of the initial CdS QDs. For the CdS:Sm (2%)/ZnS core/shell sample, the size of the particles is about 7 nm, indicating that the ZnS shell has grown successfully on the CdS:Sm core. The lattice constant of ZnS is 0.54 nm, therefore, the thickness of ZnS in CdS:Sm (2%)/ZnS QDs is about 3 monolayers.[29] The epitaxial growth of the shell over the core depends on various factors including temperature, precursor ratio, and pH, *etc.* The images reveal that the core/shell QDs are well dispersed in the solvent.

4.1.2. XRD pattern. The structural characteristics of the synthesized undoped CdS QDs, CdS doped with different concentrations of Sm^{3+} (0.5–2%), and core/shell CdS/ZnS QDs doped with Sm (2%) were determined by XRD and the results are presented in Fig. 2. The diffraction peaks of the undoped CdS QDs at $2\theta \sim 27.16°$, 44.16°, and 51.91° correspond to the [111], [220] and [311] planes, respectively. These peaks are characteristic of the cubic structure.[30] The characteristic peaks of the other phases are not observed, indicating the high purity of the product. Compared to the diffraction peaks of the undoped CdS QDs, those of the CdS:Sm (0.5%) QDs associated with the [311] plane shift slightly towards the higher angle, suggesting that the crystal is shrinking with the increase in the Sm^{3+} doping. The incorporation of Sm dopant does not change the basic crystal structure of the CdS QDs but it causes the shrinkage and distortion of the crystal lattice. Thus, the doping is achieved through the substitution of the dopant into the position of the component of the host material. Substitution doping is favorable when the ionic radii of the elements are comparable and also depends on the dopant concentration.[31] The substitutional doping takes place when the concentration of the dopant is below the solubility limit, while interstitial doping dominates when the concentration is above the solubility limit, resulting in the formation of another structure.[32,33] The relative intensity of the [220] and [311] planes of Sm-doped CdS QDs increases with an increase in the concentration of Sm^{3+} ions, while that of the [111] plane remains unaltered. The difference may be due to the preferential growth of the crystal along the [220] and [311] directions.

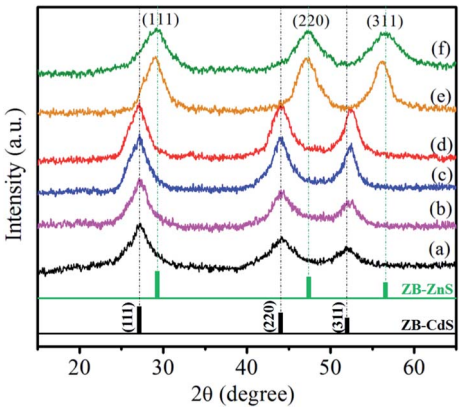

Fig. 2 XRD pattern of (a) CdS, (b) CdS:Sm0.5%, (c) CdS:Sm1%, (d) CdS:Sm2%, (e) CdS:Sm2%/ZnS, and (f) ZnS QDs.

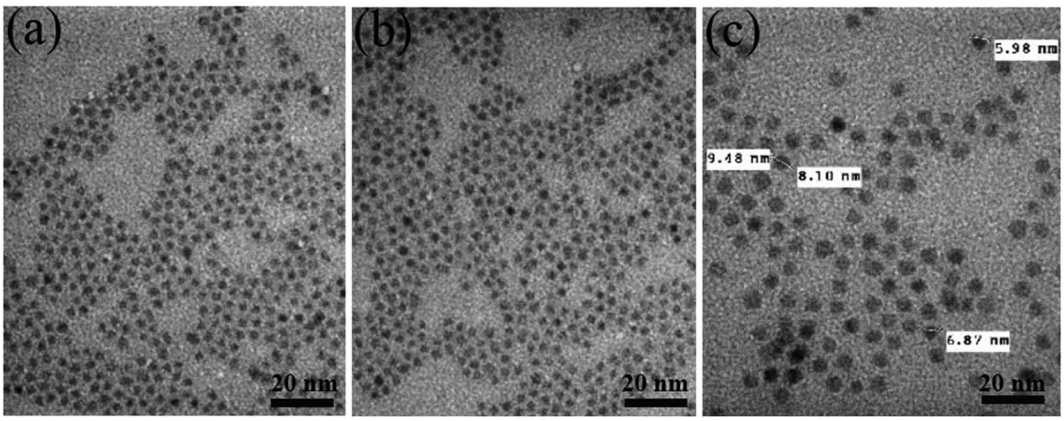

Fig. 1 TEM images of (a) CdS, (b) CdS:Sm2%, and (c) CdS:Sm2%/ZnS QDs.

The crystallite size of the synthesized nanostructures was calculated by using Debye Scherrer's formula:[33,34]

$$D = \frac{k\lambda}{\beta \cos \theta}, \quad (1)$$

where D is the crystallite size, λ is the X-ray wavelength (0.154 nm), k is the Scherrer constant (0.9), β and θ are the full width at half maximum of the diffraction peak and half diffraction angle, respectively. In this work, the calculation of the crystallite size of the QDs was based on the peak [311] because the shift of this peak towards the higher angle is observed more clearly. The lattice constant 'a' for the cubic structure was determined *via* [111] orientation using the following equation:[35]

$$\frac{1}{{d_{hkl}}^2} = \frac{h^2 + k^2 + l^2}{a^2}, \quad (2)$$

where h, k, l are the Miller indices and d_{hkl} is the interplanar space calculated from Bragg's equation: $n\lambda = 2d_{hkl} \sin \theta$. The broadening of XRD peaks is mainly due to two factors (i) size in the quantum regime and (ii) strain induced in the nanostructures. Hence, the strain was calculated using Stokes–Wilson equation:[36]

$$\epsilon = \frac{\beta \cos(\theta)}{4}. \quad (3)$$

The number of dislocations presenting in the unit area of the synthesized samples was calculated using the equation:[36]

$$\delta = \frac{1}{D^2}. \quad (4)$$

The calculated parameters from the XRD data *i.e.* D, a, d_{hkl}, δ, and ε are summarized in Table 1. The calculated values show that the crystallite size of CdS QDs increases after doping with Sm^{3+} ions. The decrease in the values of ε and δ of the QDs after doped with Sm^{3+} confirms the formation of a low-defect nanostructure.

For CdS:Sm (2%)/ZnS QDs, the diffraction peaks shift towards a higher angle, but the change in the crystalline structure is not observed after the formation of the shell. The XRD peaks for CdS:Sm (2%)/ZnS QDs observed at 28.94°, 47.20° and 56.10° correspond to the [111], [220], and [311] planes in the zinc blende structure. All the diffraction peaks systematically shift from those of the characteristics of pure CdS towards pure ZnS.[37] A similar shift in the diffraction patterns was observed during the growth of the ZnS shell on CdSe core by Dabbousi *et al.*[38] The formation of the ZnS shell over the CdS:Sm core does not affect the cubic structure of CdS, confirming the formation of core/shell QDs. The obtained values of d_{hkl} and lattice parameter 'a' are 1.61 and 5.34 nm, respectively. The reduction in d_{hkl} and lattice parameter 'a' is attributed to the smaller lattice constant of ZnS as compared to that of CdS or due to the strain induced by the shell on the core. The value of the lattice constant of CdS is larger than that of ZnS, thus, the core undergoes a compressive strain while the shell experiences a tensile strain.[39] An asymmetric internal electric field generated at the interface due to the stress induced by the lattice mismatch of the core and shell affects the electronic states and optical properties of nanostructures and will be discussed in the following sections.

4.2. Oscillation spectra and composition analysis

4.2.1. Raman spectra. It is well known that the localized electronic states of lanthanides affect the sensitive phonons of the inorganic doped material. Fig. 3 illustrates the room temperature Raman spectra of CdS QDs, CdS:Sm (2%) QDs, and CdS:Sm (2%)/ZnS QDs in the range 140–800 cm^{-1}. The spectrum of the CdS QDs contains two characteristic peaks at 296 cm^{-1} and 591 cm^{-1}, representing the characteristics of the CdS QDs attributed to the first-order (1LO) longitudinal optical phonon mode and second-order longitudinal-optical (2LO) phonon mode, respectively. The observed phonon modes of the CdS QDs shift towards the lower wavenumber *i.e.* redshift as compared to bulk material (bulk CdS (1LO) at 300 cm^{-1}). This redshift is attributed to the spatial confinement of phonons or higher strain induced by the decrease in the particle size.[40] Incorporation of Sm (2%) dopant into CdS QDs does not affect the spectra. The peaks corresponding to the structure of Sm, or its compounds are not observed. Thus, the results indicate the formation of the impurity-free samples having a reasonably

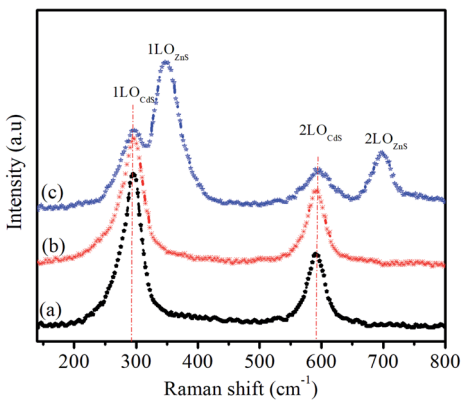

Fig. 3 RS spectra of (a) CdS, (b) CdS:Sm2%, and (c) CdS:Sm2%/ZnS QDs.

Table 1 Lattice parameters and crystallite size of CdS QDs, and Sm-doped CdS QDs QDs

S. no.	Sample	2θ	*hkl*	d_{hkl} (nm)	*a* (nm)	β	*D* (nm)	$\delta \times 10^{-2}$	$\varepsilon \times 10^{-2}$
i	CdS	51.91°	[311]	1.75	5.82	0.046	3.35	8.9	1.03
ii	CdS:Sm (0.5%)	52.17°	[311]	1.75	5.80	0.042	3.67	7.42	0.94
iii	CdS:Sm (1%)	52.29°	[311]	1.74	5.77	0.037	4.18	5.72	0.83
iv	CdS:Sm (2%)	52.43°	[311]	1.73	5.75	0.035	4.41	5.14	0.78

Table 2 Vibrational modes of Raman spectroscopy of synthesized QDs

Sample	Raman peak 1LO (cm^{-1})	Raman peak 2LO (cm^{-1})	Raman intensity (I_{1LO})	Raman intensity (I_{2LO})	Intensity ratio (I_{2LO}/I_{1LO})
CdS	296	591	43 354.2	38 888.9	0.89
CdS:Sm (2%)	296	590	45 313	42 349	0.93
CdS:Sm (2%)/ZnS	296_{CdS}, 348_{ZnS}	590_{CdS}, 696_{ZnS}	45 782_{CdS}, 49 645_{ZnS}	43 600_{CdS}, 44 559_{ZnS}	0.95_{CdS}, 0.89_{ZnS}

minor strain and bond distortion inside the lattice. The broadness of the peaks in the RS spectra confirms that the synthesized samples are in the nanoscale regime.

The intensity ratio of the overtone phonon to fundamental phonon gives the strength of the exciton–phonon coupled in semiconductors.[35] The calculated intensity ratios (I_{2LO}/I_{1LO}) of the QDs are given in Table 2. The I_{2LO}/I_{1LO} ratio of the Sm (2%) doped CdS and CdS:Sm (2%)/ZnS QDs is higher than that of the CdS QDs, suggesting that the doping and formation of the ZnS shell strengthen the exciton–phonon coupling. According to the Raman spectrum of the CdS:Sm (2%)/ZnS core/shell QDs (Fig. 3(c)), two additional peaks can be observed after the formation of the ZnS shell. The peaks at 298 cm^{-1}, 348 cm^{-1}, 596 cm^{-1} and 696 cm^{-1} are associated with 1LO (CdS), 1LO (ZnS), 2LO (CdS) and 2LO (ZnS) longitudinal optical phonon modes, respectively. The presence of the peaks of optical phonon modes of both CdS and ZnS confirms the formation of the shell. This finding is in accordance with the previously reported results.[37,41] The broadening of the peaks is due to the strain that exists at the interface of core/shell QDs.[42,43] The formation of the ZnS shell of 3 monolayers over the Sm (2%) doped CdS QDs minimizes the prominent LO peaks of CdS QDs. A similar result was reported by Bhand *et al.*[44] and can be explained by the formation of a CdSe shell over CdTe QDs. The intensity and position of the peaks change due to the structural distortion induced by the dopant or shell.

4.2.2. X-ray photoelectron spectroscopy. The surface composition and chemical states of the as-synthesized Sm (2%)

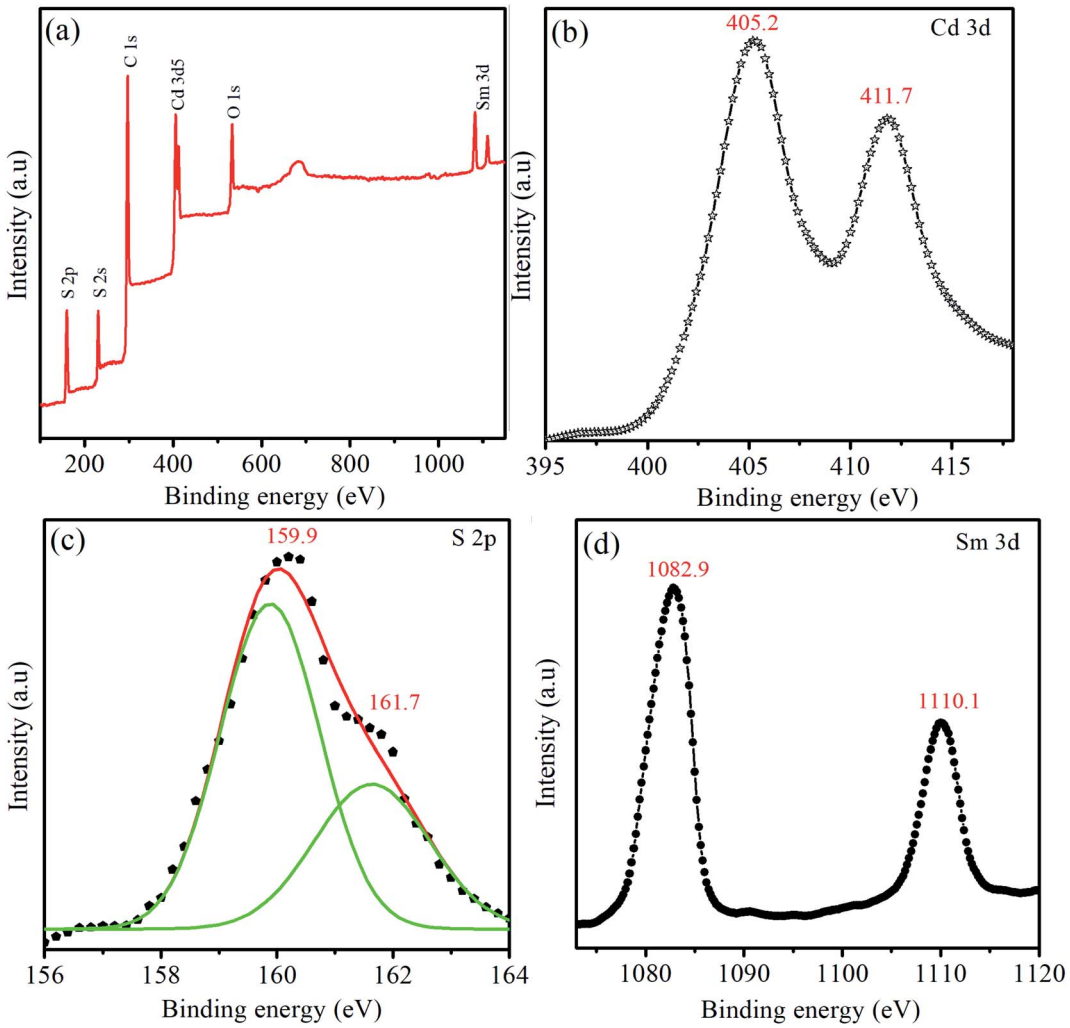

Fig. 4 (a) Survey XPS spectra of the CdS:Sm (2%) QDs, and (b) Cd 3d, (c) S 2p, (d) Sm 3d.

doped CdS QDs were analyzed by XPS and the results illustrated in Fig. 4. The presence of Cd, S, and Sm is evidenced by the appearance of the peaks of S 2p, Cd 3d, and Sm 3d. The presence of Sm 3d suggests that Sm ions were successfully doped into the CdS QD host. The spectrum also consists of peaks corresponding to C 1s and O 1s at binding energy 296.4 eV and 533 eV, respectively. The presence of the C element in the spectra is due to the hydrocarbons of the XPS instrument itself.[45]

The high-resolution XPS spectra of Cd 3d, S 2p, and Sm 3p are shown in Fig. 4(b)–(d). The strong peaks of Cd $3d_{5/2}$ and Cd $3d_{3/2}$ are observed at binding energies of 405.2 eV and 411.7 eV, respectively. The binding energy of Cd $3d_{5/2}$ attributed to the Cd^{2+} bonding state and the spin–orbit separation of 6.5 eV for Cd are in agreement with the previous data.[46] The peaks occuring in the range ~160 eV–164 eV are associated with the binding energy of S^{2-} species. For S, the peaks are fitted with Gaussian functions for the deconvolution. The high-resolution peaks of S 2p exhibit two peaks at 159.9 eV and 161.7 eV, indicating that −2 is the dominant oxidation state of S. The major peak at 159.9 eV and low-intensity peak at 161.7 eV are indexed with the $2p_{3/2}$ and $2p_{5/2}$ states of S, respectively. When compared to the binding energy of S 2p in bulk CdS, that in CdS:Sm QDs shows a blue shift which may be due to the influence of quantum confinement effect.[47]

For Sm 3d, the two peaks with an energy difference of 27.2 eV observed at the binding energy of 1082.9 eV and 1110.1 eV are attributed to Sm $3d_{3/2}$ and $3d_{5/2}$, respectively. The binding energy of the Sm 3d appearing at 1082.9 eV corresponds to the energy of Sm^{3+} photoelectrons. The concentrations of Cd, Sm, and S in the CdS:Sm2% QDs calculated from Cd 3d, Sm 3d, and S 2p signals are 57.7, 1.4, and 40.9%, respectively.

4.3. Optical properties

4.3.1. PLE spectra. The excitation spectrum gives information about the characteristic absorption lines of the elements. Fig. 5(a) illustrates the excitation spectrum of the CdS:Sm2% QDs (blue line) recorded in a range of 300–600 nm at an emission wavelength of 604 nm. The series of peaks at longer wavelengths are associated with the intra-configurational f–f transitions in Sm^{3+} ions. The transitions are labeled as $^6H_{5/2} \rightarrow {}^4D_{5/2}$ (360 nm), $^6H_{5/2} \rightarrow {}^4D_{1/2}$ (378 nm), $^6H_{5/2} \rightarrow {}^6P_{3/2} + {}^4F_{7/2}$ (404 nm, the strongest band), $^6H_{5/2} \rightarrow {}^4M_{19/2}$ (418 nm), $^6H_{5/2} \rightarrow {}^4G_{9/2}$ (437 nm), $^6H_{5/2} \rightarrow {}^4I_{11/2,13/2}$ (474 nm), $^6H_{5/2} \rightarrow {}^4F_{3/2}$ (529 nm), and $^6H_{5/2} \rightarrow {}^4G_{9/2}$ (565 nm). These results indicate that the Sm-doped CdS QDs can be excited using a broad range of excitation wavelengths. The excitation spectrum of CdS:Sm2%/ZnS QDs (red line) also has similar excitation peaks of Sm^{3+} ions, however, these peaks are sharper. This proves that the fluorescence properties of the CdS:Sm2% QDs are enhanced by the ZnS shell.

The absorption (Abs) spectra of the CdS and CdS:Sm2% QDs are presented in the inset of Fig. 5(b). On the Abs spectrum of the CdS QDs (blue line), the first excitonic absorption peak can be observed at a wavelength of 425 nm, corresponding to the lowest energy transition between the ground hole and electron ($1S_{3/2}(h)$–$1S(e)$). It can be used to estimate the diameter of the QDs according to Yu's empirical equation:[48] $D = (-6.6521 \times 10^{-8})\lambda^3 + (1.9557 \times 10^{-4})\lambda^2 + (1.6242 \times 10^{-3})\lambda^2 - (9.2352 \times 10^{-1})\lambda + 13.29$, where λ is the wavelength of the first excitonic absorption peak D is the size of QDs. In this study, the estimated size of the QDs is about 4.2 nm. Some characteristic absorption peaks of Sm ions can be seen on the Abs spectrum of the CdS:Sm2% QDs (red line), which are similar to PLE spectra. We can see a slight shift of the first excitonic absorption peak of CdS:Sm2% QDs (see the red line in Fig. 5(b)) towards longer wavelengths compared to that of CdS QDs. This slight redshift may be due to the larger size of CdS:Sm2% QDs when compared to that of CdS QDs. This assumption is consistent with the size of the QDs given in Table 1.

4.3.2. Photoluminescence spectra. PL spectra provide information regarding the electronic transitions associated with the dopant or impurities presenting in the samples. Fig. 6(a) shows the PL spectra of CdS QDs, Sm^{3+} (0.5–2%) doped CdS QDs and CdS:Sm (2%)/ZnS QDs. The spectra are recorded in 400 nm–800 nm range with an excitation wavelength of

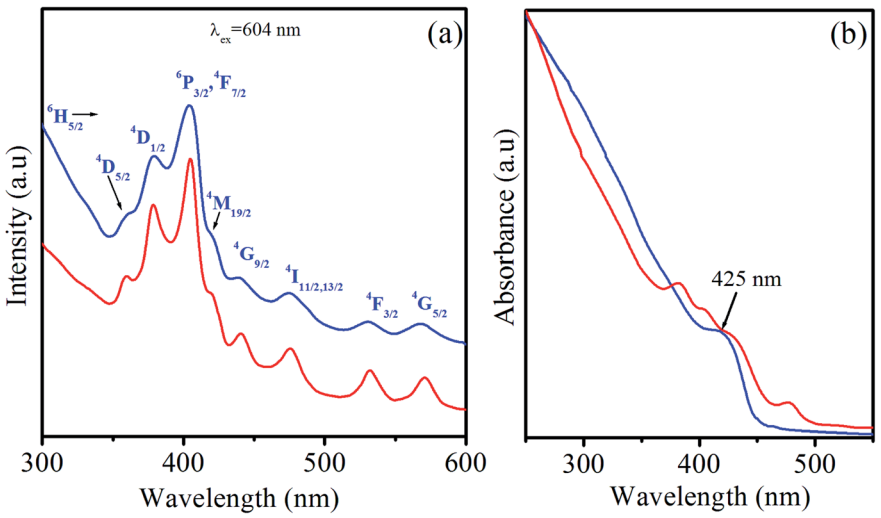

Fig. 5 (a) PLE spectra of CdS:Sm2% QDs (blue line) and CdS:Sm2%/ZnS core/shell QDs (red line). (b) UV-vis absorption spectra of CdS (blue line) and CdS:Sm2% QDs (red line).

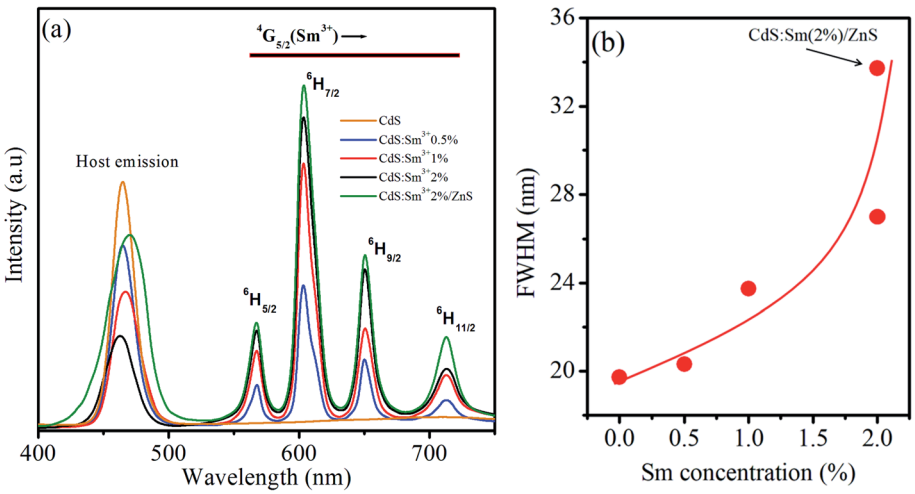

Fig. 6 (a) PL spectra (b) FWHM of host emission peak of CdS, CdS:Sm (0.5–2%) and CdS:Sm2%/ZnS QDs.

378 nm ($^6H_{5/2} \rightarrow {}^4D_{1/2}$ transition). The spectrum of the CdS QDs consists of a sharp emission peak in the blue region (420–490 nm) centred at 465 nm associated with the band to band edge emission arising from electron–hole recombination. This peak is blue-shifted when compared to the peak of the CdS bulk which is at about 500 nm. A broad hump observed in the range of 550 nm–800 nm is assigned to the recombination *via* surface localized states.[49] The luminescent spectra of lanthanide-doped semiconductor QDs are caused by the radiative transition from intra-4f electrons of triply ionized lanthanides. Therefore, they are promising materials for light emitters.

For the CdS QDs doped with Sm^{3+} (0.5%), the spectrum consists of one band at 465 nm and four new peaks located in the region of 550–750 nm. The peak in the blue region centred at 465 nm is due to the CdS host. The intensity of the peak due to the band edge emission of CdS QDs centred at 465 nm decreases after the incorporation of Sm^{3+} ions. This quenching is owing to the shallow traps caused by the introduction of new defect levels and lattice defects after Sm doping, which can trap photo-generated electrons and promote the separation of electrons and holes. The intensity of PL depends on various factors including the morphology of the nanostructures, change/energy transfer between the dopant and semiconductor, and the origin of new defect levels. The four new peaks centred at 567 nm, 604 nm, 650 nm, and 713 nm are due to the transitions in Sm^{3+} ions. These peaks are associated with f–f forbidden transitions of the 4f electrons of Sm^{3+}. It can be seen that the emission band of the CdS host (445–490 nm) overlaps with the $^6H_{5/2} \rightarrow {}^4G_{9/2}$ and $^6H_{5/2} \rightarrow {}^4I_{11/2,13/2}$ excitation bands of Sm^{3+} ions (see Fig. 5 and 6). This indicates an obvious possibility of the energy transfer process from CdS QDs to Sm^{3+} ions as illustrated in Fig. 7. In this process, Sm^{3+} ions at the ground state can be excited to $^4G_{9/2}$ or $^4I_{11/2,13/2}$ levels through reabsorbing photons that are emitted by the band–band transition. Then, the Sm^{3+} ions relax non-radiatively to the $^4G_{5/2}$ level. Finally, they relax to the ^6H_J levels by emitting the Sm^{3+} characteristic radiations in the range from 550 to 750 nm. This energy transfer process also contributes to the luminescent quenching of the CdS host.

As shown in Fig. 6, the most intense peak for Sm-doped CdS QDs is observed at 604 nm, while the weak emissions are observed at 567 and 713 nm. The emission results show that doping II–VI QDs with lanthanides gives the emission spectrum in the entire visible region. When the electromagnetic field interacts with the electron of an atom, the allowed emission transitions occur because of the electronic dipole, electronic quadrupole, or magnetic dipole. The peaks observed at 567, 604, 650, and 713 nm are contributed to the $^4G_{5/2}$–$^6H_{5/2}$, $^4G_{5/2}$–$^6H_{7/2}$, $^4G_{5/2}$–$^6H_{9/2}$, and $^4G_{5/2}$–$^6H_{11/2}$ transitions of Sm^{3+} ions states, respectively. Xiao *et al.*[50] observed similar transitions in Sm^{3+}-doped $CaWO_4$ nanoparticles. The emission structure can be described by taking into account that the ^6H_J levels are divided into $2J + 1$ sublevels in the crystal field.[51] The allowed transition for the magnetic dipole follows $\Delta J = 0, \pm 1$. Therefore, the first transition $^4G_{5/2}$–$^6H_{5/2}$ follows the magnetic dipole character and the second transition $^4G_{5/2}$–$^6H_{7/2}$ follows the magnetic dipole character as it obeys the selection rule, but the electric dipole character dominates in this transition, and $^4G_{5/}$

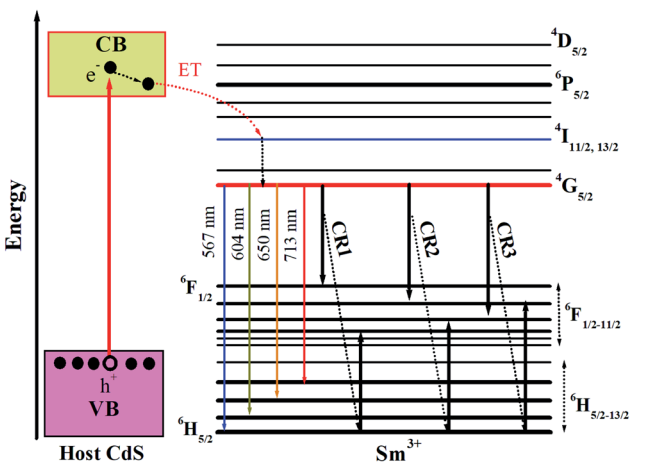

Fig. 7 Schematic illustration of the energy transfer mechanism from host CdS to Sm.

$_2$–$^6H_{9/2}$ demonstrates pure electric character. Therefore, the transition at 650 nm is hypersensitive to the crystal field.

Knowledge about the local symmetry of the crystal can be gathered by finding the intensity ratio of the electric dipole transition to the magnetic dipole transition. The emission intensity ratio at 650 nm to 567 nm is found to be 1.59, indicating that the electric dipole transition dominates the magnetic dipole transition, thus asymmetry of the Sm^{3+} ion sites is possible in the crystal structure. For Sm (2%) doped CdS QDs, the change in the ratio of the electric dipole to the magnetic dipole is highest, suggesting an increase in the asymmetry. The relative intensities of these transitions are very sensitive to the variations in the local environment of Sm^{3+} ions. The energy transfer between CdS QDs and Sm^{3+} ions takes place *via* electron exchange or coulombic mechanism and also depends on the distance between the donor and the acceptor.

The effect of the concentration of Sm^{3+} ions on CdS QDs has been studied using luminescent spectra. As the concentration of Sm^{3+} ions changes (0.5%, 1%, and 2%), the position of the emission peaks remains unchanged, but the intensity is affected. The increase in the concentration of dopant ions in CdS QDs quenches the host emission (peak about 465 nm). This quenching is due to the increasing ion–ion interactions between Sm^{3+} ions, leading to an increase in the non-radiative process and causing concentration-dependent quenching.[52,53] The increase in the concentration of Sm^{3+} ions in CdS QDs enhances the emission peaks caused by Sm^{3+} ions. This enhancement in the emission peaks is originated from the growth of luminescent centers. The emission spectrum of CdS:Sm (2%)/ZnS QDs consists of five emission bands. The peak observed at the band edge shows a redshift of ~5 nm as compared to that of CdS QDs and Sm-doped CdS QDs. This shift is due to the tunneling of charge carriers into the ZnS shell. The peak centred at 470 nm shows an increase in the emission of CdS:Sm after passivating the QDs with the ZnS shell. The spectrum of CdS:Sm (2%)/ZnS QDs also consists of emission peaks of Sm^{3+} ions with the enhanced emission intensity. Coating the Sm^{3+}-doped CdS QDs with the ZnS shell suppresses the recombination by passivating surface nonradiative recombination sites. A redshift of the emission peak and an enhancement in its FWHM are observed after the CdS QDs were coated with the ZnS shell.

Fig. 6(b) depicts the change in FWHM value with the change in the concentration of dopant and with the formation of the ZnS shell. It can be seen that the FWHM values of all the samples are in a narrow range (from 18 to 34 nm) and that of the CdS:Sm (2%)/ZnS QDs is the highest. The enhancement in the emission of CdS:Sm (2%)/ZnS core/shell QDs can be associated with an interband connection between the interface of the core and the disordered shell. The ZnS shell confines the photogenerated e^-–h^+ to the CdS core interface, resulting in the passivation of the nonradiative transitions and enhancing the luminescence intensity.[54] These results indicate that the synthesized QDs are a promising red-emitting material for white-light LED applications.

As shown in Fig. 6, the emission intensity of Sm^{3+} ions in the CdS:Sm^{3+}/ZnS QDs is higher than that in the CdS:Sm^{3+} QDs. This behavior may be originated for two reasons. The first one relates to the change of the local environment of Sm^{3+} ions. Some authors reported that Zn^{2+} can diffuse into the CdS lattice during the formation of the ZnS shell over the CdS:Sm^{3+} QD core.[55,56] In this case, Zn^{2+} ions play a role as a modifier component in the CdS matrix. The appearance of the Zn^{2+} modifier in CdS QDs may increase the asymmetry of the ligand field of Sm^{3+} ions, leading to an enhancement of the radiative transition probability from $^4G_{5/2}$ levels,[57] *i.e.*, an increase in emission intensity from this level. The second reason relates to the decrease of surface states. It is known that the QDs always contain the surface states which create the continuum energy levels in the band gap of materials. These levels are usually in a wavelength range of 500–750 nm for CdS and ZnS QDs. The energy band of the surface states overlaps the transition energy of the Sm^{3+} emission bands. Thus, the photons emitted by the Sm^{3+}:$^4G_{5/2}$ → ^6H_J (J = 5/2, 7/2, 9/2, and 11/2) transitions may be reabsorbed by the surface states. This process constrains the increase of the Sm^{3+} luminescent bands. However, coating ZnS shell over CdS:Sm^{3+} QDs decreases the surface defect, leading to the decrease of the energy transfer process from Sm^{3+} to the surface states. This creates the increase of the Sm^{3+}:$^4G_{5/2}$ → ^6H_J emission bands in the CdS:Sm^{3+}/ZnS QDs in comparison with those of the CdS:Sm^{3+} QDs.

It can be seen that the increase of the $^4G_{5/2}$ → $^6H_{11/2}$ emission band at 713 nm is significantly higher than that of other bands. Coating ZnS shell over CdS:Sm^{3+} QDs does not remove completely the surface states, *i.e.*, the energy transfer process from Sm^{3+} to the surface states of both CdS core and ZnS shell still exists in CdS:Sm^{3+}/ZnS QDs. Nevertheless, the lowest energy level of the ZnS surface states in the CdS:Sm^{3+}/ZnS QDs (1.77 eV) is higher than 1.74 eV (713 nm), so the probability of the 713 nm photon absorption is significantly lower than that of the photons having absorption wavelengths of 567, 604 and 650 nm. This is the reason why the increase in the intensity of the $^4G_{5/2}$ → $^6H_{11/2}$ transition (713 nm) in the CdS:Sm^{3+}/ZnS QDs is larger than that of other transitions.

4.3.3. Emission decay curve. To understand more about the luminescent characteristics of the synthesized QDs, the fluorescent kinetic measurements were carried out. Fig. 8 illustrates the emission decay curves of the CdS QDs doped with Sm^{3+} (0.5–2%) and CdS:Sm (2%)/ZnS QDs. The luminescent decay of the CdS:Sm^{3+} (with different Sm concentrations) and core/shell QDs was monitored at $^4G_{5/2}$–$^6H_{9/2}$ transition (604 nm) with an excitation wavelength of 525 nm. The obtained data of the samples were fitted with a biexponential function and the results are presented in Fig. 8. The curves show a typical PL decay at room temperature, which is multi-exponential. The equation used for exponential decay is given as $F(t) = A_0 + \sum_{i=1}^{n} A_i \exp\left(-t/\tau_i\right)$, where A_i is the pre-exponential factor, and τ_i is the lifetime. The average lifetime is calculated using the equation:[58,59]

$$\tau_{av} = \sum_{i=1}^{n} A_i \tau_i^2 \Big/ \sum_{i=1}^{n} A_i \tau_i.$$

The values of the decay lifetime and fitness of curve R^2 obtained by fitting are summarized in Table 3. The fast component (τ_1) is associated with luminescence from defect states in the CdS QDs

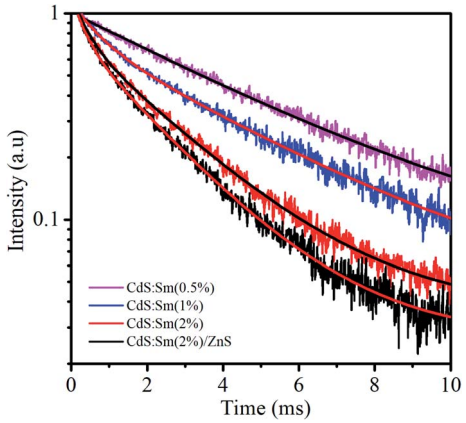

Fig. 8 Emission decay curves for CdS:Sm (0.5–2%) and CdS:Sm2%/ZnS QDs under excitation wavelength at 525 nm and the emission wavelength at 604 nm. Solid lines represent the fitting curves to a multiexponential function.

while the slow component (τ_2) is ascribed to the $^4G_{5/2}$–$^6H_{7/2}$ transition of Sm^{3+} ions.[60] For CdS:Sm^{3+} QDs, it can be seen that the average lifetime decay constant decreases with the increase in Sm concentration. This value is 4.45 ms with an Sm^{3+} concentration of 0.5%, decreases to 3.75 ms with a concentration of 1%, and falls to 2.09 ms when the dopant concentration is 2%. The long decay time is induced by a forbidden transition of Sm^{3+} according to a spin selection rule. The lifetime decay of the order of ms is sufficient for applications in displays.[61,62]

The quenching of the lifetime of Sm^{3+}:$^4G_{5/2}$ level relates to the energy transfer process through cross-relaxation (CR) between Sm^{3+} ions.[63] Some energy transfer channels between Sm^{3+} ions are illustrated in Fig. 7. In this process, an Sm^{3+} ion in excited level ($^4G_{5/2}$) would transfer its energy to a neighbor ion in the ground state ($^6H_{5/2}$), then both two ions enter the energy levels from $^6H_{7/2}$ to $^6F_{1/2}$. Finally, they relax to the ground level through a mutilphonon process or an infrared emission. Thus, luminescence and lifetime of $^4G_{5/2}$ level are quenched.

As mentioned in Section 4.3.2, coating CdS:Sm^{3+} QDs by ZnS leads to the increase of the radiative transition probability of Sm^{3+}:$^4G_{5/2}$ level and the decrease of energy transfer probability from Sm^{3+} ion to surface states. It is known that the lifetime of any exciting level is the inverse of the total transition probability (including the radiative and energy transfer processes) from that level.[57] The lifetime of $^4G_{5/2}$ level in CdS:Sm^{3+}/ZnS QDs is smaller than that in CdS:Sm^{3+} QDs, *i.e.*, the total transition probability from $^4G_{5/2}$ level in CdS:Sm^{3+} QDs is enhanced by coating ZnS. This indicates that the increase of Sm^{3+} radiative probability by Zn^{2+} diffusion effect has largely dominated the decrease of energy transfer probability from Sm^{3+} to surface states.

Table 3 Lifetime decay constants and fitness of curves

Sample	τ_1 (ms)	τ_2 (ms)	$\langle\tau\rangle$ (ms)	R^2
CdS:Sm (0.5%)	4.45 (50%)	4.45 (50%)	4.45	0.994
CdS:Sm (1%)	4.00 (67.9%)	0.69 (32.1%)	3.75	0.996
CdS:Sm (2%)	2.45 (63.8%)	0.39 (36.2%)	2.09	0.997
CdS:Sm (2%)/ZnS	2.14 (63.6%)	0.36 (36.4%)	1.98	0.998

4.4. Effect of storage time on fluorescent properties

To evaluate the optical stability of the synthesized QDs under normal storage conditions (in toluene and darkness), the emission properties of the CdS QDs, Sm (2%) doped CdS QDs and Sm (2%) doped CdS/ZnS QDs were studied after 47 days, and 376 days after fabrication of samples. Fig. 9 shows the effect of aging on the CdS QDs, CdS:Sm (2%) QDs, and CdS:Sm (2%)/ZnS core/shell QDs. The synthesized CdS QDs show a sharp emission peak centred at 465 nm and a broad hump in the range 550–750 nm. The peak at a lower wavelength corresponds to the band edge emission (recombination of holes and electrons), while the peak at a higher wavelength is due to the recombination *via* surface localized states. In the sample after 47 days of fabrication, the band edge emission peak shifts towards a higher wavelength centred at 466.6 nm and the relative intensity decreases by 17.27%. The intensity of the hump in the range of 550–750 nm increases. Similarly, for the sample after 376 days, the band edge emission peak quenches to a large extent with a large redshift, while the peak at a higher wavelength dominates. The peak at band edge emission is quenched with aging owing to the increase in non-radiative transitions. The intensity of hump at a higher wavelength is enhanced because of the increase in the defect levels.[57,59]

For the CdS:Sm (2%) QDs, the emission spectra of the as-synthesized QDs show a peak at 462.6 nm associated with band edge emission of the CdS host. The peaks observed at 567 nm, 603 nm, 650 nm, and 713 nm correspond to the transitions in energy levels of Sm^{3+} dopant. After 47 days of fabrication, the relative intensity of all the emission peaks associated with the CdS QDs and Sm^{3+} ions decreases. After 376 days, the emission peaks are quenched completely, implying the complete degradation of the Sm-doped QDs.

Impressive long-term stability is observed in the case of the CdS:Sm (2%)/ZnS core/shell QDs. After 47 days of fabrication, the relative intensity of the emission peak associated with the band edge emission does not show any significant shift. Besides, the relative intensity at 470 nm only falls by 1.25%. After 376 days of fabrication, there is a small shift of ~3 nm in the band edge emission peak towards a higher wavelength, and the relative

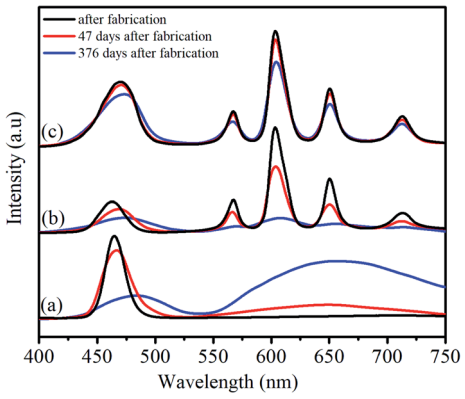

Fig. 9 PL spectrum of (a) CdS, (b) CdS:Sm 2%, and (c) CdS:Sm 2%/ZnS QDs according to storage time.

intensity falls by only 5.5%. Thus, the emission studies reveal that core/shell QDs maintain 94.5% of their emission intensity even after 376 days of storage under ambient conditions. There is no significant change in the position of the emission peaks after 47 days of fabrication. A similar trend has been observed for the peaks located in the range of 550–713 nm. Thus, the results indicate that the ZnS shell completely passivates the Sm-doped CdS cores and protects them from oxidative environment and degradation.

5. Conclusion

A series of Sm-doped CdS QDs were synthesized using a facile and simple wet chemical method. The CdS:Sm (2%) QDs were coated with three monolayers of ZnS. The synthesized Sm-doped CdS QDs are spherical with an average size of 4 nm and not affected by the dopant. The synthesized CdS QDs exhibit a cubic structure. The incorporation of dopant follows a substitutional doping mechanism and does not change the structure of the host. With the formation of the ZnS shell over the CdS:Sm (2%) QD core, the particle size of the QDs increases, and characteristic XRD peaks shift toward the higher angles but the cubic structure of QDs remains unchanged. The emission spectra of Sm-doped CdS QDs consist of five peaks including one peak at 465 nm corresponding to the band edge emission of CdS and four peaks at 567 nm, 605 nm, 650 nm, and 713 nm attributed to the f–f transitions in Sm^{3+} ions dominated by electric dipole $^4G_{5/2}$–$^6H_{9/2}$ transition at 650 nm. The increase of the dopant concentration significantly reduces the host emission intensity but enhances the emission efficiency of Sm^{3+} ions due to the ET from host to dopant and the cross-relaxation between Sm^{3+} ions. The synthesized Sm-doped CdS QDs exhibit broad excitation spectra, therefore the QDs of different colors can be excited using a single wavelength. Raman spectra confirm the formation of single-phase QDs and show that the formation of shell induces strain over the core/shell interface. The effect of aging shows that the formation of ZnS shell gives long term stability with 94.5% of emission efficiency retained after 376 days of storage. The decay lifetime of the fabricated QDs is in the order of milliseconds makes them potential for display applications.

Conflicts of interest

There are no conflicts to declare.

Acknowledgements

This research is funded by the Vietnam National Foundation for Science and Technology Development (NAFOSTED) under grant number 103.02-2017.350.

References

1 N. X. Ca, N. Q. Bau, T. L. Phan, V. T. K. Lien, N. T. T. Lieu and N. X. Nghia, *J. Alloys Compd.*, 2017, **697**, 401–408.
2 N. Amjad and F. Huaxiang, *J. Comput. Theor. Nanosci.*, 2009, **6**, 1277–1289.
3 N. Zeiri, A. Naifar, S. A. B. Nasrallah and M. Said, *Chem. Phys. Lett.*, 2020, **744**, 137215.
4 Y. Li, E. C. Y. Liu, N. Pickett, P. J. Skabara, S. S. Cummins, S. Ryley, A. J. Sutherland and P. O'Brien, *J. Mater. Chem.*, 2005, **15**, 1238–1243.
5 P. Praus, L. Svoboda, J. Tokarsky, A. Hospodkova and V. Klemm, *Appl. Surf. Sci.*, 2014, **292**, 813–822.
6 L. Liu, S. Hu, Y. Pan, J. Zhang, Y. Feng and X. Zhang, *Beilstein J. Nanotechnol.*, 2014, **5**, 919–926.
7 M. Darwish, A. Mohammadi and N. Assi, *Mater. Res. Bull.*, 2016, **74**, 387–396.
8 C. Li, J. H. Zhao, X. Chen, F. Y. Li, X. L. Zhang, Z. G. Chen and Q. D. Chen, *Semicond. Sci. Technol.*, 2020, **35**, 015019.
9 F. Xu, Y. Zhao, M. Hu, P. Zhang, N. Kong, R. Liu, C. Liu and S. K. Choid, *Chem. Commun.*, 2018, **54**, 9525–9528.
10 X. Wang, S. Chen, S. Thota, Y. Wang, H. Tan, M. Tang, Z. Quan and J. Zhao, *J. Phys. Chem. C*, 2019, **123**, 19238–19245.
11 O. Amiri, S. M. H. Mashkani, M. M. Rad and F. Abdvali, *Superlattices Microstruct.*, 2014, **66**, 67–75.
12 H. Kumar, P. B. Barman and R. R. Singh, *Phys. E*, 2015, **67**, 168–177.
13 X. Xu, Y. Yang, H. Jin, B. Pang, R. Yang, L. Yan, C. Jiang, D. Shao and J. Shi, *ACS Sustainable Chem. Eng.*, 2020, **8**, 6806–6814.
14 S. Bharti, G. Kaur, S. Jain, S. Gupta and S. K. Tripathi, *J. Drug Targeting*, 2019, **27**, 813–829.
15 H. T. Van, N. D. Vinh, P. M. Tan, U. T. D. Thuy, N. X. Ca and N. T. Hien, *Opt. Mater.*, 2019, **97**, 109392.
16 R. P. Panmand, S. P. Tekale, K. D. Daware, S. W. Gosavi, A. Jha and B. B. Kale, *J. Alloys Compd.*, 2020, **817**, 152696.
17 K. V. Chandekar, M. Shkir, A. Khan and S. AlFaify, *Mater. Sci. Semicond. Process.*, 2020, **118**, 105184.
18 K. T. Ranjit, H. Cohen, I. Willner, S. Bossmann and A. M. Braun, *J. Mater. Sci.*, 1999, **34**, 5273–5280.
19 V. X. Quang, P. V. Do, N. X. Ca, L. D. Thanh, V. P. Tuyen, P. M. Tan, V. X. Hoa and N. T. Hien, *J. Lumin.*, 2020, **221**, 117039.
20 A. G. Khosroshahi and A. Mehrizad, *J. Mol. Liq.*, 2019, **275**, 629.
21 S. B. Ubale, T. T. Ghogare, V. C. Lokhande, T. Ji and C. D. Lokhande, *SN Appl. Sci.*, 2020, **2**, 756.
22 N. S. Rao, M. Rajesh, K. Prasad, G. R. Reddy, B. D. P. Raju and S. Dhanapandian, *Lumin*, 2020, **35**, 1–7.
23 P. V. Do, V. X. Quang, L. D. Thanh, V. P. Tuyen, N. X. Ca, V. X. Hoa and H. V. Tuyen, *Opt. Mater.*, 2019, **92**, 174–180.
24 K. Ashwini, C. Pandurangappa, K. Avinash, S. Srinivasan and E. Stefanakos, *J. Lumin.*, 2020, **221**, 117097.
25 Q. Xiao, Z. Si, Z. Yu and G. Qiu, *Mater. Sci. Eng., B*, 2007, **137**, 189–194.
26 J. C. Sin, S. M. Lam, K. T. Lee and A. R. Mohamed, *J. Colloid Interface Sci.*, 2013, **401**, 40–49.
27 P. M. Tan, N. X. Ca, N. T. Hien, H. T. Van, P. V. Do, L. D. Thanh, V. H. Yen, V. P. Tuyen, Y. Peng and P. T. Tho, *Phys. Chem. Chem. Phys.*, 2020, **22**, 6266–6274.
28 N. X. Ca, N. T. Hien, P. M. Tan, T. L. Phan, L. D. Thanh, P. V. Do, N. Q. Bau, V. T. K. Lien and H. T. Van, *J. Alloys Compd.*, 2019, **791**, 144–151.

29 U. Hotje, C. Rose and M. Binnewies, *Sol. Sta. Sci.*, 2003, **5**, 1259–1262.
30 G. Chena, B. Yi, G. Zenga, Q. Niua, M. Yana, A. Chena, J. Dua, J. Huanga and Q. Zhang, *Colloids Surf., B*, 2014, **117**, 199–205.
31 M. A. Manthrammel, M. Shkir, S. Shafik, M. Anis and S. AlFaify, *J. Mater. Res.*, 2020, **35**, 410–421.
32 N. X. Ca, N. T. Hien, N. T. Luyen, V. T. K. Lien, L. D. Thanh, P. V. Do, N. Q. Bau and T. T. Pham, *J. Alloys Compd.*, 2019, **787**, 823–830.
33 P. T. Tho, N. D. Vinh, H. T. Van, P. M. Tan, V. X. Hoa, N. T. Kien, N. T. Hien, N. T. K. Van and N. X. Ca, *J. Phys. Chem. Solids*, 2020, **139**, 109332.
34 I. E. Kolesnikov, E. V. Golyeva, M. A. Kurochkin, E. Y. Kolesnikov and E. Lähderanta, *J. Lumin.*, 2020, **219**, 116946.
35 L. Saravanan, R. Jayavel, A. Pandurangan, L. J. Hsin and M. H. Yuan, *Mater. Res. Bull.*, 2014, **52**, 128–133.
36 A. Khan, M. Shkir, M. A. Manthrammel, V. Ganesh, I. S. Yahia, M. Ahmed, A. M. El-Tonia, A. Aldalbahi, H. Ghaithan and S. AlFaify, *Ceram. Int.*, 2019, **45**, 10133–10141.
37 C. V. Reddy, J. Shim and M. Cho, *J. Phys. Chem. Solids*, 2017, **103**, 209–217.
38 B. O. Dabbousi, J. R. Viejo, F. V. Mikulec, J. R. Heine, H. Mattoussi, R. Ober, K. F. Jensen and M. G. Bawendi, *J. Phys. Chem.*, 1997, **101**, 9463–9475.
39 A. B. Sharma, S. K. Sharma, M. Sharma, R. K. Pandey and D. S. Reddy, *Spectrochim. Acta*, 2009, **72**, 285–290.
40 B. Schreder, C. Dem, M. Schmitt, A. Materny, W. Kiefer, U. Winkler and E. Umbach, *J. Raman Spectrosc.*, 2003, **34**, 100–103.
41 P. Balaz, M. Balaz, E. Dutkova, A. Zorkovska, J. Kovac, P. Hronec, J. Kovac Jr, M. Caplovicova, J. Mojzis, G. Mojzisova, A. Eliyas and N. G. Kostova, *Mater. Sci. Eng., C.*, 2016, **58**, 1016–1023.
42 N. X. Ca, V. T. K. Lien, N. X. Nghia, T. T. K. Chi and T. L. Phan, *Nanotechnology*, 2015, **26**, 445701.
43 S. Parani, N. Tsolekile, K. Pandian and O. S. Oluwafemi, *J. Mater. Sci.: Mater. Electron.*, 2017, **28**, 11151.
44 G. R. Bhand and N. B. Chaure, *Mater. Sci. Semicond. Process.*, 2017, **68**, 279–287.
45 R. Rajendran, K. Varadharajan and V. Jayaraman, *Colloids Surf., A*, 2019, **580**, 123688.
46 R. Rajendran, V. Jayaraman and K. Varadharajan, *J. Phys. Chem. Solids*, 2019, **129**, 261–269.
47 N. Kakuta, J. M. White, A. Campion, A. J. Bard, M. A. Fox and S. E. Webber, *J. Phys. Chem.*, 1985, **89**, 48–52.
48 W. W. Yu, L. Qu, W. Guo and X. Peng, *Chem. Mater.*, 2003, **15**, 2854–2860.
49 N. X. Ca, H. T. Van, P. V. Do, L. D. Thanh, P. M. Tan, N. X. Truong, V. T. K. Oanh, N. T. Binh and N. T. Hien, *RSC Adv.*, 2020, **10**, 25618.
50 Q. Xiao, Q. Zhou and M. Li, *J. Lumin.*, 2010, **130**, 1092–1094.
51 V. V. Ursaki, V. Lair, L. Zivkovic, M. Cassir, A. Ringuede and O. Lupan, *Opt. Mater.*, 2012, **34**, 1897–1901.
52 Y. Liu, C. Zhai, K. Zhang, L. Du, M. Zhu and M. Zhang, *J. Magn. Magn. Mater.*, 2020, **503**, 166618.
53 K. Swapna, S. Mahamuda, A. S. Rao, S. Shakya, T. Sasikala, D. Haranath and G. V. Prakash, *Spectrochim. Acta, Part A*, 2014, **125**, 53.
54 C. Zhai, H. Zhang, N. Du, B. Chen, H. Huang, Y. Wu and D. Yang, *Nanoscale Res. Lett.*, 2011, **6**, 1–5.
55 D. Shaw, *J. Cryst. Growth*, 1988, **86**, 778.
56 Z. Jiang and D. F. Kelley, *J. Phys. Chem. C*, 2013, **117**, 6826–6834.
57 B. M. Walsh, *Judd-Ofelt theory: principles and practices*, Springer, Dordrecht, 2006, pp. 403–433, ISBN 978-1-4020-4789-3, DOI: 10.1007/1-4020-4789-4_21.
58 N. X. Ca, N. T. Hien, P. N. Loan, P. M. Tan, U. T. D. Thuy, T. L. Phan and Q. B. Nguyen, *J. Electron. Mater.*, 2019, **48**, 2593–2599.
59 N. T. Hien, T. T. K. Chi, N. D. Vinh, H. T. Van, L. D. Thanh, P. V. Do, V. P. Tuyen and N. X. Ca, *J. Lumin.*, 2020, **217**, 116822.
60 C.-W. Wang and M. G. Moffitt, *Langmuir*, 2004, **20**, 11784–11796.
61 G. Dong, X. Xiao, Y. Chi, B. Qian, X. Liu, Z. Ma, S. Ye, E. Wu, H. Zeng, D. Chen and J. Qiu, *J. Phys. Chem. C*, 2009, **113**, 9595–9600.
62 R. Yu, H. M. Noh, B. K. Moon, B. C. Choi, J. H. Jeong, H. S. Lee, K. Jang and S. S. Yi, *J. Lumin.*, 2014, **145**, 717–722.
63 V. X. Quang, N. N. Dat, V. P. Tuyen, N. M. Khaidukov, V. N. Makhov, L. D. Thanh, N. X. Ca, N. T. Thanh, P. T. T. Nga and P. V. Do, *Opt. Mater.*, 2020, **107**, 110049.